

MOOSE Simulation Project: Part 3

Gwen White

March 2025

1 Introduction

This project involved using the MOOSE[3] (Multiphysics Object Oriented Simulation Environment) simulation framework to model the temperature profile of elements within a fuel rod. These elements include a fuel pellet, gap, and cladding. The first part of this project models the temperature profiles of steady-state and transient systems with both constant thermal conductivity and temperature-dependent thermal conductivity. The simulation object used here was a 2-D representation of one half of a fuel rod in order to easily model how heat conducts radially from the inside of the fuel pellet to the outer cladding. The axial (Z) and radial (R), dimensions for each element were given as seen in Figure 1. The materials for each element were not given, but the selected materials were uranium dioxide UO_2 as fuel, helium (He) as the gap and Zirconium (Zr) as the cladding as they are commonly used materials in fuel rods. [1] The second part of this project models the temperature profile for the following parts of the fuel rod: outer cladding surface, fuel surface, and fuel centerline. Since the model in part 2 incorporates axial heat transport and a fluctuating coolant temperature a steady state temperature dependent thermal conductivity setup was used to support accurate temperature gradients. Lastly, the axial location of the peak fuel centerline temperature was identified. The geometry of the model remained the same from part 1, except for the length of the fuel rod increased to 100 cm to more accurately model a fuel rod. The third part of this project expanded the model to include thermal-mechanical coupling. Thermal expansion and fuel swelling were added to simulate how the fuel grows over time as it heats up and accumulates burnup. As fuel swells, it eventually closes the gap and comes into contact with the cladding. This results in mechanical stresses between the fuel and cladding, that will be used to predict when cracking of the fuel will occur.

1.1 Simulation Setup

1.2 Mesh

The coordinate system 'RZ' was used to model the 2-D axisymmetric geometry of a fuel rod. Although the systems with constant thermal conductivity could

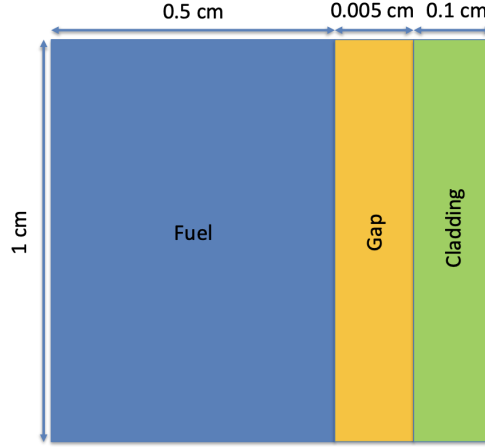


Figure 1: 2-D schematic of the fuel rod model used in Parts 1 and 3, where UO_2 is the fuel, He is the gap, and Zr is the cladding.

be treated as 1-D problems, 2-D modeling was needed to capture variations in both the radial and axial directions when using a temperature-dependent conductivity. Since heat is generated in the fuel and conducted radially outward, higher resolution in the radial direction was needed compared to the axial. I ran a range of simulations with different n_x and n_y values and compared the results to an analytical temperature profile calculated in Python. As shown in Figure 2, $n_x=400$, $n_y=4$ provided a good match without overshooting the analytical results, so that resolution was used for Part 1. Ideally, refining the mesh should make the solution converge toward the analytical profile. However, at very fine meshes, I noticed slight divergence, which suggests numerical errors or convergence issues in the simulation. A time derivative kernel was added for the transient simulations. For Part 2, the same mesh setup was used, except the axial resolution was increased to $n_y = 100$ to account for the longer 100 cm fuel rod. Higher axial resolution was needed to capture changes in temperature along the length, while the radial resolution stayed the same since material properties remained uniform and heat flow in the radial direction was still the most dominant. In Part 3, the mesh was divided into three separate submeshes for the fuel, gap, and cladding. Dimensions stayed consistent with earlier parts, and all distances were in centimeters. I used $n_x=50$, $n_y=8$ for the fuel and cladding, and $n_x=20$, $n_y=8$ for the gap. The submeshes were stitched together using the `StitchedMeshGenerator`, which kept fuel boundary names intact for applying boundary conditions later. Separating the mesh made it easier to assign different mechanical properties like thermal expansion, elasticity, and swelling, which became important once thermal-mechanical coupling was added.

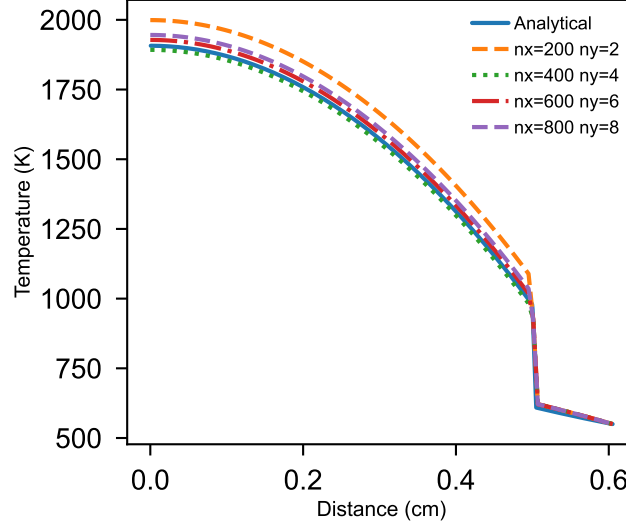


Figure 2: Comparison of steady state temperature profiles of systems with varying mesh resolutions to the analytically solved temperature profile. All temperature profiles are holding thermal conductivity constant.

1.3 Variables and Functions

The heat conduction equations, which solve for temperature as a function of space and time in all of the systems, are solved using the first order finite element approximation. The heat conduction equations do differ between steady state 1 and transient 2 systems however, since temperature varies with time in the transient systems. The transient heat conduction equation also requires the heat capacity and density of each material as these properties effect the heating and cooling rates for each material.

$$0 = \nabla \cdot (k \nabla T) + Q \quad (1)$$

$$\rho c_p \frac{\partial T}{\partial t} = \nabla \cdot (k \nabla T) + Q \quad (2)$$

The applied heat source in part 1 is represented by the Volumetric Heat Rate (VHR) which calculates the amount of heat generated through the length of the material (or fuel rod). The VHR for steady-state systems is constant (350 W/m²) and represents a uniform heat source. The VHR for the transient systems 3 is modeled by a Gaussian function that varies with time since this system is time dependent. This function represents a heat generation rate that peaks at $t = 20$ s and decays over time.

$$\text{VHR}(t) = 350 \times \exp\left(\frac{-(t - 20)^2}{2}\right) + 350 \quad (3)$$

For the second part of this project, the Linear Heat Rate (LHR) and coolant temperature function T_{coolant} are implemented to account for axial heat transfer and the effect of on the outer cladding temperature. The LHR function ensures that the heating distribution between the fuel rod elements is more realistic and not uniform along the rod. The coolant temperature function provides a dynamic boundary condition that responds to variations in heat generation, better reflecting actual reactor conditions. These functions help capture the interaction between heat generation and coolant absorption more effectively, making the model behave more similar to real world reactor conditions.

First, the Linear Heat Rate (LHR) in W/cm was converted into a Volumetric Heat Rate (VHR) using the fuel cross-sectional area:

$$\text{VHR}(z) = \frac{\text{LHR}(z)}{\pi R_{\text{fuel}}^2} \quad (4)$$

where R_{fuel} is the fuel radius.

The LHR profile was modeled using a cosine shape:

$$\text{LHR}(z) = 350 \cos \left(1.2 \left(\frac{z}{50} - 1 \right) \right) \quad (5)$$

The coolant boundary temperature was modeled as:

$$T_{\text{coolant}}(z) = 500 + \frac{350 \cos \left(1.2 \left(\frac{z}{50} - 1 \right) \right)}{2\pi R_{\text{fuel}} 2.65} + \frac{1}{1.2} \left(\frac{50 \times 350}{250 \times 4.2} \right) \left(\sin(1.2) + \sin \left(1.2 \left(\frac{z}{50} - 1 \right) \right) \right) \quad (6)$$

For Part 3, mechanical behavior was modeled to account for fuel swelling, thermal expansion, and stress buildup over time. Stresses were calculated using isotropic linear elasticity, with eigenstrains added for thermal expansion and swelling. Thermal strain was based on the temperature difference from a reference temperature, and swelling was modeled as a function of burnup and temperature using a DerivativeParsedMaterial. The solver tracked the radial, hoop, and axial stress components separately, which helped show how different types of stress built up inside the fuel. After gap closure, hoop stress became the dominant stress component.

$$k_{\text{fuel}}(T, BU) = \frac{1}{(3.8 + 200 \times BU) + 0.0217 \times T} \quad (7)$$

$$BU(t) = \frac{\text{LHR}}{\pi R_{\text{fuel}}^2 \rho_{\text{fuel}} E_{\text{fission}}} \times t \quad (8)$$

1.4 Materials

For the materials, UO_2 was used as fuel, He as the gap, and Zr as a cladding, since these are all commonly used reactor materials. The densities, heat capacities, and thermal conductivities for UO_2 [2], Zr [4] and He [5] were all found in

Material	k (W/cm·K)	ρ (g/cm ³)	c_p (J/g·K)
UO ₂	0.03	10.98	0.33
Helium	0.0015	0.1786×10^{-3}	5.19
Zirconium	0.17	6.5	0.35

Table 1: Materials and Their Properties Used in Simulation

literature and declared within each material so they could be used to calculate the heat conduction equations.

For the temperature-dependent thermal conductivity systems we use equation 9 for the fuel, equation 10 for the gap, and equation 11 for the cladding.

$$k_{\text{fuel}}(T) = \frac{100}{7.5408 + 17.629 \frac{T}{1000} + 3.6142 \left(\frac{T}{1000}\right)^2 + 6400 \left(\frac{T}{1000}\right)^{5/2} \exp\left(\frac{-16.35}{T/1000}\right)} \quad (9)$$

$$k_{\text{gap}}(T) = 16 \times 10^{-6} \cdot T^{0.79} \quad (10)$$

$$k_{\text{cladding}}(T) = 8.8527 + 7.0820 \times 10^{-3} \cdot T + 2.5329 \times 10^{-6} \cdot T^2 + 2.9918 \times 10^3 \cdot \frac{1}{T} \quad (11)$$

In Part 3, materials were modeled to account for thermal-mechanical coupling effects. An isotropic linear elastic model was applied to each material region to represent mechanical behavior. Fuel swelling from fission gas accumulation was modeled using a DerivativeParsedMaterial function. This function calculated a swelling eigenstrain as a combined function of burnup and temperature, based on existing experimental data from irradiated UO₂. The resulting strain caused volumetric growth of the fuel, which led to gap closure and the buildup of mechanical stresses over time. As seen in Table 2, the helium gap had a very low stiffness and a Poisson's ratio of zero, allowing it to easily deform and be compressed or closed by the expanding fuel over time.

Material	E (GPa)	ν	α (K ⁻¹)
UO ₂	200	0.345	11×10^{-6}
Helium	1×10^{-9}	0.0	N/A
Zirconium	80	0.41	7.1×10^{-6}

Table 2: Mechanical Properties and Thermal Expansion Coefficients Used for Each Material Region

1.5 Boundary Conditions

Different boundary conditions were applied to the left and right sides of the model. The left side of the system uses the Neumann 13 boundary condition.

The Neumann boundary condition makes the heat flux zero at the specified boundary to maintain radial symmetry. Since the radial axis is symmetric at this location, this a zero heat flux boundary is appropriate. The Neumann boundary condition is also applied to the top and bottom of the system to ensure that the transfer of heat is isolated along the length of the rod. The right side, where the outer cladding is, uses the Dirichlet Boundary condition. The Dirichlet 12 Boundary holds a specified temperature value constant at the boundary which is consistent with the outer surface of our cladding that is held at a constant temperature of 550 K. The constant temperature is used to mimic the coolant surrounding a fuel rod in a reactor. For part 2 of this project, only a functional Dirichlet boundary condition was applied to the right side of the model. The difference between the functional Dirichlet boundary and the standard Dirichlet boundary condition is that it allows the temperature to fluctuate based on the cooling temperature function, rather than having a fixed temperature for the boundary condition. This supports a more accurate model as it resembles the temperature fluctuations reflects the effect of coolant on the cladding temperature, where a constant cladding temperature can not. In Part 3, similar thermal boundary conditions to Parts 1 and 2 were used to maintain symmetry, isolate heat transfer along the rod, and hold a constant temperature on the outer cladding surface to represent the coolant. In addition, however, a Dirichlet condition was applied to the bottom of the rod to prevent vertical displacement. This helps keep the system mechanically stable by removing rigid body motion in the axial direction, which makes sense since in a real reactor the bottom of the fuel rod would be physically supported.

$$u = g \quad \text{on } \partial\Omega_D \quad (12)$$

$$\frac{\partial u}{\partial n} = h \quad \text{on } \partial\Omega_N \quad (13)$$

2 Executioner

For the executioner, steady state or transient was applied, depending on the system type being simulated. For transient systems, an iterative time stepper was added to adjust the time step based on the simulation rather than using a constant time step value.

3 Results

$$\sigma_{\theta\theta}(\eta) = -\sigma^* (1 - 3\eta^2) \quad (14)$$

$$\sigma^* = \frac{\alpha E(T_0 - T_s)}{4(1 - \nu)} \quad (15)$$

$$\eta = \frac{r}{R_f} \quad (16)$$

From figure 3, we can see that the curve of the analytical and modeled constant thermal conductivity curves are very similar. Both have peaks of 1800 K at the centerline temperature and decrease in temperature as you move from inside the pellet out towards the helium gap. The sharp drop in temperature around 0.5 cm occurs right at the helium gap then slowly decreases down to 550 K where it reaches the outer cladding. The steady-state temperature for the temperature-dependent thermal conductivity system shows a similar trend but with a slightly lower temperature profile through the fuel, starting at 1750 K but still finishing around 550 K at the outer cladding. Ideally, a temperature-dependent thermal conductivity should lower the centerline temperature even more compared to the constant conductivity case. The small difference seen here is likely due to how the boundary conditions were applied and some mesh effects in the model. This behavior suggests that reducing the effective thermal conductivity at higher temperatures lowers the heat flux through the material, but the current setup may have muted the expected difference between cases.

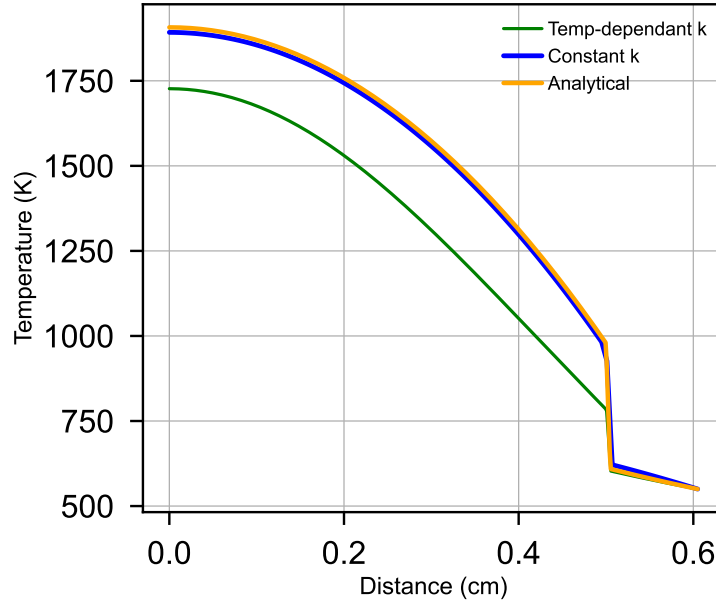


Figure 3: Temperature profile for three steady-state modeling approaches: (1) an analytical solution, (2) a numerical solution with constant thermal conductivity (K), and (3) a numerical solution with temperature-dependent thermal conductivity.

Figure 4 shows the centerline temperature over a specified time interval of 0 to 100 seconds. For both constant and temperature-dependent thermal conductivity systems, the temperatures increase from 0 K to 1600 K in the first 20 seconds. Around 23 seconds, the centerline temperature sharply increases

to a max temperature of 1971.3 K for the constant conductivity model and 2005.3 K for the temperature-dependent model. After peaking, both curves dip slightly and then settle around 1758 K. This shows that at higher temperatures, temperature-dependent conductivity drives a quicker initial rise in temperature, but has less influence after the system reaches equilibrium. Again, a bigger difference between the curves would normally be expected, but the way the boundary conditions were set up likely made them look closer than they should.

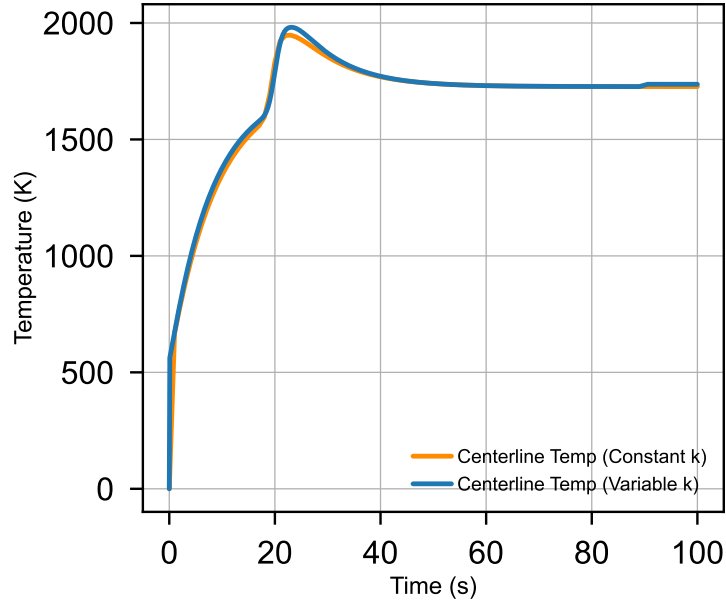


Figure 4: Centerline temperature over time of transient systems.

Figure 5 shows the centerline temperature along the axial direction of the fuel rod for the fuel surface, fuel centerline, and cladding surface. The parabolic shape of the plots shows that for all elements within the fuel rod the temperature is highest around the middle (halfway up the rod). In reality, the peak centerline temperature would be expected to shift slightly upward toward the outlet, due to the effect of the coolant flowing along the rod. In this case, the maximum temperature appears around 50 cm, likely because the boundary condition for the cladding was treated more like a constant value instead of varying with height. Even so, the general temperature trends match expectations, and the peak centerline temperature of 1720.93 K is consistent with the values seen in figures 3 and 4.

For Part 3, thermal-mechanical effects were added to the model to look at how the fuel swells, closes the gap, and builds up stress over time.

Figure 9 shows how the average burnup of the fuel increases steadily over time as the fission reactions occur and more energy is released. The continuous

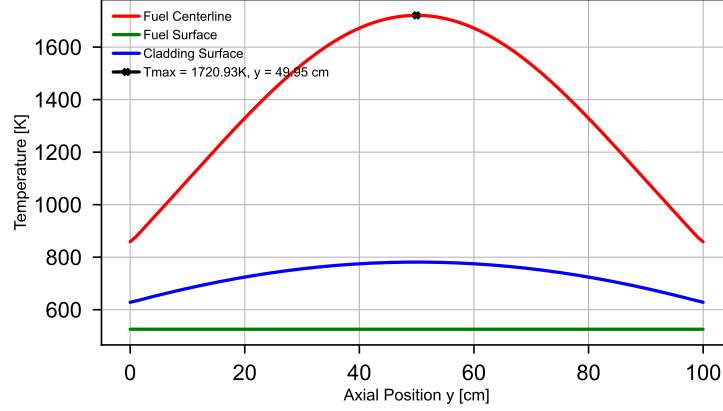


Figure 5: Axial temperature profiles of the fuel centerline, fuel surface, and outer cladding surface. The max centerline temperature of 1720.93 K was calculated and plotted at a distance of 50 cm. This is at steady-state conditions and the thermal conductivities are temperature-dependent.

increase in burnup is what results in fuel swelling as it causes more fission gas to release and solid fission products to be produced. Figure 6 shows that the radial displacement is larger than axial displacement throughout the simulation. This is because the swelling and thermal expansion push outward toward the cladding. This radial growth is what leads to the eventual closure of the gap. Figure 7 shows the shrinking of the fuel-cladding gap width over time. It is observed that the gap width decreases until it reaches zero at around 0.5×10^8 seconds. This corresponds to about 578 days, or roughly 1.6 years of operation time. This is a reasonable time scale considering that many reactor fuel cycles last around 18–24 months before refueling [6]. Figure 8 shows how the average radial, axial, and hoop stresses evolve over time. Early in the simulation, stresses are low because the fuel is free to expand into the gap. After the gap closes, hoop stress rapidly rises and becomes the dominant stress component. This is because after closure, the fuel can no longer expand outward easily and internal pressures build up. The hoop stress peaks near the outer radius of the fuel, which is where thermal cracking is likely to occur once stress exceeds material fracture limits. Radial stress becomes slightly compressive, and axial stress stays lower overall but still grows over time.

The crack radius was estimated using the following hoop stress model:

$$\sigma_{\theta\theta}(\eta) = -\sigma^*(1 - 3\eta^2) \quad (17)$$

where the peak stress is given by

$$\sigma^* = \frac{\alpha E(T_0 - T_s)}{4(1 - \nu)} \quad (18)$$

and the normalized radius is

$$\eta = \frac{r}{R_f}. \quad (19)$$

Using the peak centerline temperature $T_0 = 1720$ K, surface temperature $T_s = 550$ K, thermal expansion coefficient $\alpha = 11 \times 10^{-6} \text{ K}^{-1}$, Young's modulus $E = 200$ GPa, and Poisson's ratio $\nu = 0.345$, the normalized crack radius was calculated to be $\eta = 0.5315$. This corresponds to a physical radius of approximately $r_{\text{crack}} = 0.2657$ cm, meaning thermal cracking would likely start just past halfway from the center of the fuel pellet. This matches the stress distribution shown in Figure 10, where hoop stress peaks near $\eta = 0.5$. The high hoop stress near the outer radius supports that thermal cracking would likely begin in this region after gap closure.

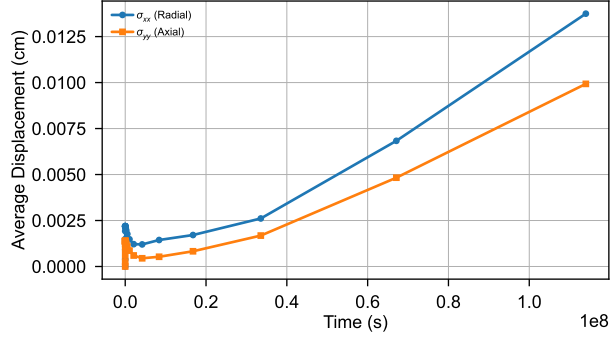


Figure 6: Average radial and axial displacement of the fuel over time. Radial displacement is larger because the fuel expands outward more than it stretches axially.

4 Conclusions

In this project, MOOSE was used to simulate the axial and radial temperature profiles of a fuel rod and show the significance of thermal conductivity on steady-state and transient behavior. In steady-state conditions, temperature-dependent conductivity led to higher overall temperatures due to reduced heat flux. In transient systems, it caused a faster centerline temperature rise but had little effect after about 30 seconds as the system approached equilibrium. The axial temperature profile analysis in Part 2 showed that the hottest location in the rod occurs where the linear heat rate is highest. Functional boundary conditions and mesh resolution choices were also important for accurately capturing temperature distributions. In Part 3, thermal-mechanical coupling was added to model fuel swelling, thermal expansion, and stress development. Fuel expansion

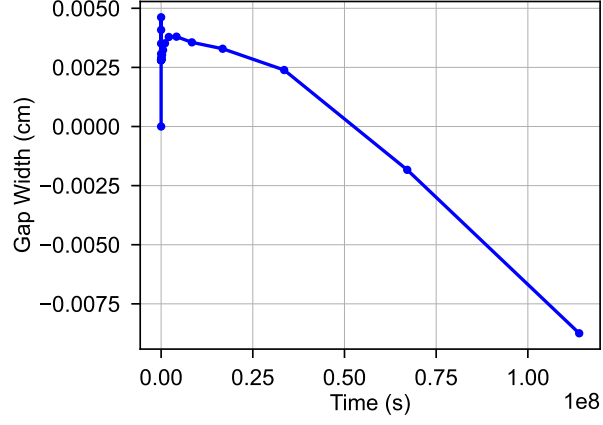


Figure 7: Gap width between the fuel and cladding as a function of time. The gap gradually closes as the fuel swells and expands.

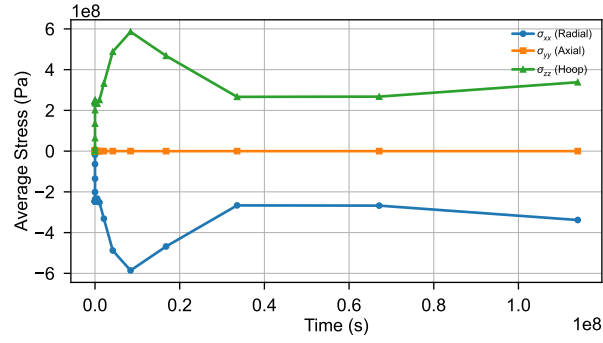


Figure 8: Evolution of average radial, axial, and hoop stresses in the fuel over time. Hoop stress sharply rises and dominates after gap closure.

led to early gap closure and a buildup of mechanical stresses, with hoop stress becoming dominant. The hoop stress exceeded typical fracture limits, suggesting that cracking would likely occur under these conditions. Modeling these effects allowed for a more realistic prediction of fuel behavior beyond thermal conduction alone.

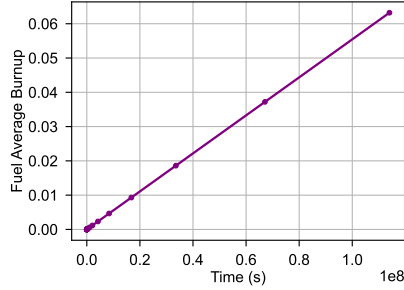


Figure 9: Fuel average burnup as a function of time. Burnup increases steadily throughout the simulation, driving fuel swelling.

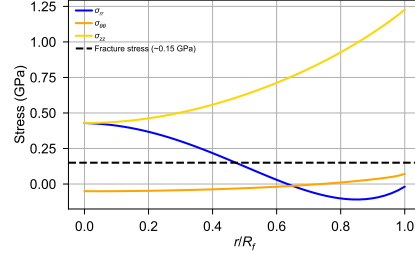


Figure 10: Evolution of average radial, axial, and hoop stresses over the normalized radius.

References

- [1] CR de F Azevedo. Selection of fuel cladding material for nuclear fission reactors. *Engineering Failure Analysis*, 18(8):1943–1962, 2011.
- [2] Juan J Carbajo, Gradyon L Yoder, Sergey G Popov, and Victor K Ivanov. A review of the thermophysical properties of mox and uo2 fuels. *Journal of Nuclear materials*, 299(3):181–198, 2001.
- [3] Giudicelli et al. 3.0 - MOOSE: Enabling massively parallel multiphysics simulations. *SoftwareX*, 26:101690, 2024.
- [4] JK Fink and L Leibowitz. Thermal conductivity of zirconium. *Journal of Nuclear Materials*, 226(1-2):44–50, 1995.
- [5] John J Hurly and Michael R Moldover. Ab initio values of the thermophysical properties of helium as standards. *Journal of research of the National Institute of Standards and Technology*, 105(5):667, 2000.
- [6] Neil E Todreas and Mujid S Kazimi. *Nuclear Systems Volume I: Thermal Hydraulic Fundamentals*. CRC Press, 2021.